Optics Letters

Long-range surface plasmon polariton detection with a graphene photodetector

Ho-Seok Ee,[1,5] You-Shin No,[2] Jinhyung Kim,[3] Hong-Gyu Park,[4] and Min-Kyo Seo[3,*]

[1]Department of Physics, Kongju National University, Gongju 32588, South Korea
[2]Department of Physics, Konkuk University, Seoul 05029, South Korea
[3]Department of Physics and Institute for the NanoCentury, Korea Advanced Institute of Science and Technology, Daejeon 34141, South Korea
[4]Department of Physics and KU-KIST Graduate School of Converging Science and Technology, Korea University, Seoul 02841, South Korea
[5]e-mail: hsee@kongju.ac.kr
*Corresponding author: minkyo_seo@kaist.ac.kr

Received 13 April 2018; revised 15 May 2018; accepted 17 May 2018; posted 21 May 2018 (Doc. ID 328112); published 13 June 2018

We present an integration of a single Ag nanowire (NW) with a graphene photodetector and demonstrate an efficient and compact detection of long-range surface plasmon polaritons (SPPs). Atomically thin graphene provides an ideal platform to detect the evanescent electric field of SPPs extremely bound at the interface of the Ag NW and glass substrate. Scanning photocurrent microscopy directly visualizes a polarization-dependent excitation and detects the SPPs. The SPP detection responsivity is readily controlled up to ~17 mA/W by the drain-source voltage. We believe that the graphene SPP detector will be a promising building block for highly integrated photonic and optoelectronic circuits.

OCIS codes: (140.3490) Lasers, distributed-feedback; (250.5403) Plasmonics; (230.5160) Photodetectors; (130.0130) Integrated optics; (130.0250) Optoelectronics; (130.3120) Integrated optics devices.

https://doi.org/10.1364/OL.43.002889

Recent advances in the synthesis and characterization of low-dimensional materials such as nanowires (NWs) and nanoparticles have offered, in addition to semiconductor fabrication techniques, considerable opportunities for exploring fundamental optical phenomena and facilitating high-performance optoelectronic devices [1–5]. In particular, metallic nanomaterials allow strong concentrations of electromagnetic fields at the metal/dielectric interface, known as surface plasmon polaritons (SPPs) [6]. Plasmonic resonances at the subwavelength regime enable nanoscale device elements such as light sources, waveguides, routers, and switches for ultracompact photonic and optoelectronic circuitry [7–13]. These plasmonic devices can operate faster than their semiconductor electronic counterparts [14]. However, the seamless integration of the plasmonic and electronic elements remains a challenge because it requires an efficient conversion of SPP signals to electrical signals.

Graphene-based optoelectronics offers an ideal platform to address this issue [15–21]. The gapless graphene sensitively absorbs light over a wide range of spectrum and readily generates charge carriers [18,19]. The high carrier mobility ensures an ultrafast conversion of photons/plasmons to electrical currents/voltages [20,21]. Furthermore, a single atomic layer with high mechanical flexibility and environmental robustness makes it the best candidate for the ultimate miniaturization of a photonic-integrated circuit. In this Letter, we integrate a graphene photodetector with a bottom-up synthesized single Ag NW for direct detection of long-range SPPs. The atomically thin graphene layer introduced at the interface between the Ag NW and dielectric substrate is ideal for absorbing the evanescent electric field of SPPs and generating photocarriers with high mobility. The applied source-drain voltage enables a successful separation and collection of these carriers and increases the SPP photoresponsivity.

Figure 1(a) shows a schematic illustration of the graphene photodetector integrated with a single Ag NW. The focused incident light on one end of the NW excites the propagating SPPs at the interface between the Ag NW and the dielectric substrate. Graphene located at the NW-dielectric interface efficiently absorbs the propagating SPPs and generates electron–hole pairs. The generated charge carriers are collected in the form of a photocurrent by the source and drain electrodes of the graphene SPP detector. To calculate the field concentration of the propagating SPPs at the NW-dielectric interface, we performed the finite-difference time-domain (FDTD) simulation. The Ag NW has a circular cross section with a diameter of 200 nm, and the Drude model describes the optical response of Ag [22]. The refractive index of the SiO_2 substrate is set to 1.5. Figure 1(b) shows a plot of the calculated electric field energy depending on the vertical position across the center of the NW (white dotted line, inset). At a wavelength of 633 nm, ~16% (~26%) of the electric field energy is concentrated within 10 nm (20 nm) from the Ag/SiO_2 interface. This strong electric field energy concentration enables an efficient detection of the propagating SPPs, even from the atomically thin graphene layer. The simulation also shows that the horizontal (vertical) component of the electric field carries ~41% (~59%) of the electric field energy at the plane of the graphene layer.

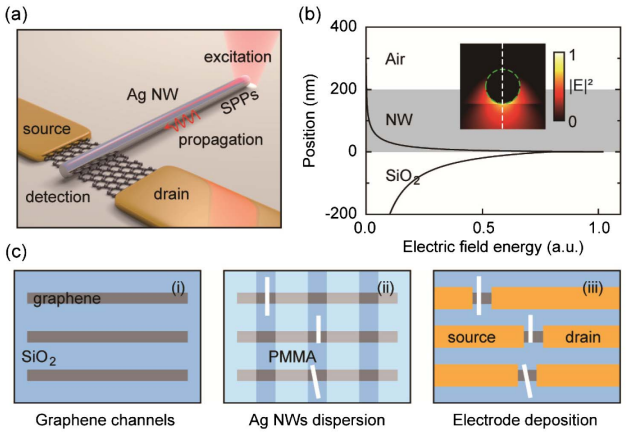

Fig. 1. (a) Schematic of the graphene SPP detector integrated with a single Ag NW. (b) Calculated vertical distribution of the electric field energy density of SPPs guided by the cylindrical Ag NW on the SiO_2 substrate ($n_{SiO2} = 1.5$). Inset: calculated cross-sectional electric field intensity distribution. The white dashed line indicates the scanning direction of the vertical distribution. The diameter of the NW is 200 nm. The propagation length of the SPPs is calculated to be ~16 μm. (c) Device fabrication steps: (i) formation of graphene channels on the SiO_2 substrate, (ii) directional dispersion of the Ag NWs along PMMA trenches, and (iii) deposition of source and drain electrodes.

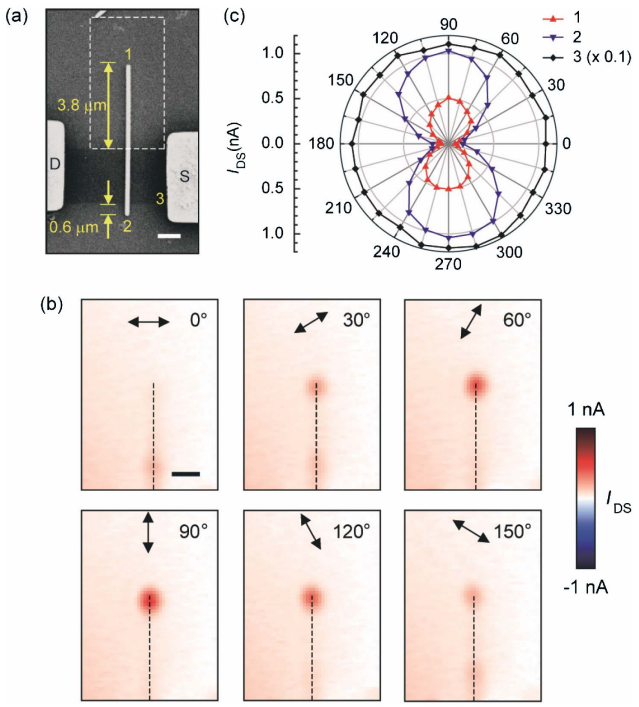

Fig. 2. (a) SEM image of the fabricated graphene SPP detector integrated with a single Ag NW. Scale bar, 1 μm. (b) Photocurrent distribution depending on the polarization angle of the incident laser in the white dotted box in (a). Scale bar, 1 μm. (c) Polarization-dependent photocurrent measurements at three different positions in (a): 1 (red triangle, the upper end), 2 (blue inverted triangle, the lower end) and 3 (black diamond, near the source electrode). The incident laser power is 2 mW, and no drain-source voltage is applied.

The graphene layer absorbs the horizontal electric field and generates the photocarriers.

The key fabrication steps of the Ag NW-coupled graphene SPP detector are illustrated in Fig. 1(c). First, a graphene monolayer grown by chemical vapor deposition was transferred to a receiving SiO_2 (300 nm)/Si substrate and patterned by electron beam lithography followed by O_2 plasma etching to define multiple graphene channels [(i), the leftmost]. Secondly, poly (methyl methacrylate) (PMMA) trenches perpendicular to the graphene channels were defined by additional electron beam lithography to facilitate the directional dispersion of the Ag NWs dissolved in ethanol vertical to the graphene channel [(ii), center]. After the NW dispersion, the PMMA trenches were removed. Thirdly, electron beam evaporation and a lift-off process formed the source and drain electrodes of the Ti (20 nm)/Au (80 nm) layer [(iii), the rightmost].

A scanning electron microscopy (SEM) image in Fig. 2(a) shows the fabricated graphene photodetector integrated with a single Ag NW. The vertically aligned Ag NW had a diameter of 200 nm and a length of ~6.9 μm. The monolayer graphene channel with a width of ~2.5 μm was connected to the source and drain electrodes separated by ~4.6 μm. The upper and lower ends of the Ag NW [positions 1 and 2 in Fig. 2(a)] were ~3.8 and ~0.6 μm apart from the graphene channel, respectively. To identify SPP detection, we performed scanning photocurrent microscopy measurements. A ×50 objective focused a HeNe laser beam at 632.8 nm on an area for which the full width at half-maximum (FWHM) of intensity was ~900 nm. The photocurrent signal collected by the electrodes was analyzed by a lock-in amplifier (Stanford Research Systems, SR830) operating at a repetition rate of 7.3 kHz and a duty cycle of 50%. Using a piezo stage, we scanned the photocurrent distribution with a step size of 100 nm.

Figure 2(b) shows the measured photocurrent distributions with different incident polarizations of 0°, 30°, 60°, 90°, 120°, and 150°. The NW (the black dotted line) is aligned at a 90° angle from the horizontal direction. The incident power of the laser was 2 mW. A linear polarizer and a half-wave plate rotated the polarization angle of the incident laser without changing the intensity. The long-range propagating SPPs coupled with the incident light polarized parallel to the metal NW. In addition, the phase matching for coupling the SPPs and the free-propagating radiation could be supported only in the proximity of the end of the NW. The polarization-resolved photocurrent distribution measurements exhibited the expected excitation characteristics of the propagating SPPs. The incident light polarized perpendicular to the NW axis generated a negligible photocurrent of the background level. As the polarization angle increased, the photocurrent increased accordingly. At the polarization parallel to the NW axis, the photocurrent was maximized to 0.51 nA. The incident light focused around the NW end produced a polarization-dependent photocurrent, but the light incident on the body of the NW did not show a notable contribution to the photocurrent generation in any of the polarization states. Therefore, it is obvious that the photocurrent detected by the graphene monolayer originates from the propagating SPPs at the Ag NW/SiO_2 interface.

To confirm and evaluate the photocurrent generation by the excited SPPs, we measured the degree of polarization of

the photocurrent generated at the upper and lower ends of the NW, as shown in Fig. 2(c). We also compared the results with the polarization dependence of the direct photocurrent generation at a position on the graphene layer near the source electrode [position 3 in Fig. 2(a)]. The photocurrent measurements at the upper and lower ends of the NW show almost an identical response to the polarization state of the incident light. On the other hand, the photocurrent directly generated at the graphene layer does not exhibit polarization dependence. The difference in the polarization state of photocurrent generation between at the NW end and on the graphene layer clarifies the excitation of the propagating SPPs. We also note that the comparison of the photocurrents generated from the upper and lower ends allows an indirect estimation of the propagation length of SPPs (L_{SPP}). The maximum photocurrent of ~1.03 nA from the lower end is two times larger than that from the upper end (~0.51 nA). The longer the propagation distance, the lower is the detected photocurrent. The ratio of photocurrent between the upper and lower ends rarely changes depending on the polarization angle. Considering the distances of the upper and lower ends of the NW from the graphene channel as ~3.8 and ~0.6 μm, respectively, we estimate L_{SPP} to be ~5.2 μm, which is ~3.1 times shorter than the numerically calculated propagation length of ~16 μm. We attribute the difference between the numerical and experimental propagation lengths to surface roughness of the Ag NW and SiO_2 substrate caused during the fabrication [23] and non-ideal shapes of the Ag NW facets.

To examine the linearity of the graphene SPP detector, we measured the photocurrent depending on the incident laser power from 0.0 to 2.0 mW [Fig. 3(a)]. The measured graphene SPP detector was integrated with a 7.1 μm long Ag NW oriented by an angle of 105° with respect to the graphene channel. The lower 1.6 μm of the Ag NW is in contact with the graphene channel [inset SEM image, Fig. 3(a)], and the excited SPPs propagate at a distance of ~5.5 μm from the upper end to the graphene channel. The incident laser beam was polarized parallel to the NW axis to maximize the photocurrent generation, and the drain-source voltage (V_{DS}) was 0 V. The graphene SPP detector shows a clear linear response of photocurrent to the incident power. The slope of the plot yields the photoresponsivity of the entire system (R_{photo}); photoresponsivity is defined as the ratio of the net photocurrent ($I_{DS} - I_{dark}$) to the incident laser power (P_{inc}), which is ~0.2 μA/W in the present case. Here I_{DS} and I_{dark} represent the measured currents with and without the incident light, respectively. When no drain-source voltage is applied, no current is observed beyond the detection noise level; $I_{DS} = I_{dark} = 0$ for $V_{DS} = 0$. The applied drain-source voltage enables one to control and increase the responsivity, as shown in Fig. 3(b). The V_{DS} of 1 V results in R_{photo} of ~45 μA/W, which is ~225 times greater than the zero-bias responsivity. We note that the asymmetric location of the Ag NW to the source and drain electrodes produce a dc current of the generated photocarriers, even at the zero-bias voltage [12].

To evaluate the intrinsic behavior of the graphene SPP detector, we need to estimate the SPP detection responsivity (R_{SPP}), which is defined as the ratio of the output photocurrent to the input optical power of SPPs (P_{SPP}). The relation between R_{SPP} and R_{photo} is given as

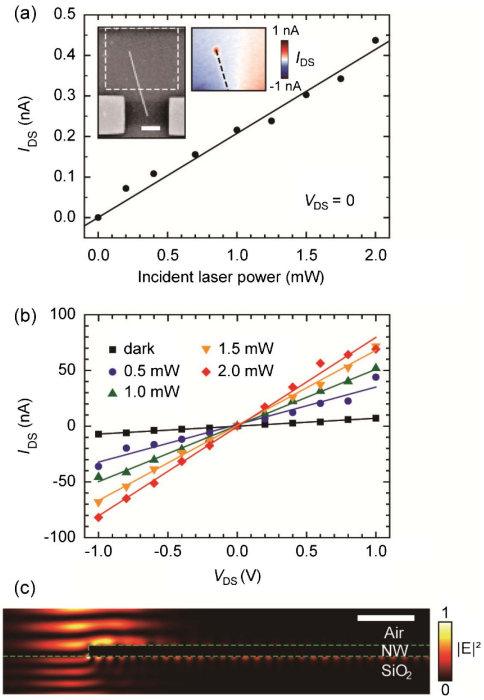

Fig. 3. (a) Measured photocurrent as a function of the incident laser power, P_{inc}, ranging from 0.2 to 2.0 mW. Here the drain-source voltage, V_{DS}, is 0 V. Insets: SEM image and scanning photocurrent distribution ($P_{inc} = 2$ mW) of the measured device. The Ag NW is oriented with an angle of ~105° to the graphene channel, and the incident light is polarized parallel to the NW axis. Scale bar, 2 μm. (b) Measured photocurrent as a function of V_{DS} with various incident powers; dark (black squares), 0.5 (navy circles), 1.0 (green triangles), 1.5 (yellow reversed triangles), and 2.0 mW (red diamonds). (c) Calculation of the coupling efficiency between the incident light and SPPs at the end of the Ag NW. We employ a Gaussian incident beam with a wavelength and spot size (FWHM in intensity) of 633 nm and 900 nm, respectively. Scale bar, 1 μm.

$$R_{SPP} = \frac{I_{DS} - I_{dark}}{P_{SPP}} = \frac{I_{DS} - I_{dark}}{P_{inc}\eta_c e^{-L/L_{spp}}} = \frac{R_{photo}}{\eta_c e^{-L/L_{spp}}}. \quad (1)$$

Here η_c is the coupling efficiency of the incident light to the propagating SPPs at the end of the Ag NW, and L is the distance of the NW end from the graphene channel. To calculate the value of $\eta_c \times \exp(-L/L_{SPP})$, we performed a three-dimensional FDTD simulation in which the Gaussian beam with an FWHM of 900 nm excites SPPs at the end of the Ag NW on SiO_2 substrate [Fig. 3(c)]. We calculated the power flux of the SPPs at a position 5.5 μm distant from the NW end and its ratio to the power of the Gaussian incidence. The power flux of the SPPs was integrated over an area of 2 μm × 2 μm involving the cross section of the NW. The calculated power flux ratio of ~0.27% was used to estimate the value of R_{SPP} which came out to be ~74 μA/W and 17 mA/W for a V_{DS} of 0 V and 1 V, respectively. We note that this is a conservative estimation assuming ideal theoretical excitation and propagation of SPPs. We expect that the responsivity could be improved by enhancing the electric field component parallel to the graphene layer further and extending the interaction length between the graphene and the propagating SPPs [21].

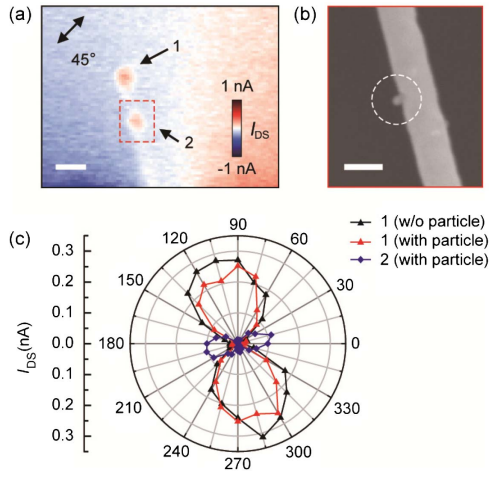

Fig. 4. (a) Photocurrent distribution of the sample of Fig. 3 three weeks later than the first measurement. Here the incident beam is linearly polarized by 45° (60° to the NW axis). Scale bar, 1 μm. (b) Magnified SEM image of the red dotted box in (a). Scale bar, 200 nm. (c) Polarization-dependent photocurrent measurements at the points 1 and 2 in (a) without (black triangles, first measurement) and with the nanoparticle (red triangles and navy diamonds, second measurement). For all the measurements, the incident laser power is 2 mW.

To demonstrate the robustness of our device's performance over time, we repeated the scanning and polarization-dependent photocurrent measurements of the same sample, as shown in Fig. 3, after a three-week interval. We kept the sample in the ambient atmosphere during the period. As seen in Fig. 4(a), the incident light with a polarization angle of 60° with respect to the NW axis generates distinctive photocurrent signals not only from the NW end (position 1), but also from a position on the NW body (position 2). The magnified SEM image in Fig. 4(b) shows that a nanoparticle with a size of ~30 nm protrudes from the NW body due to the oxidation of Ag. The nanoparticle enables the incident light to excite the propagating SPPs and generate the photocurrent. Figure 4(c) shows the polarization-dependent plots of the first (black, without nanoparticle) and the second (red and navy for position 1 and 2, with nanoparticle) photocurrent measurements. We note the following features. First, the nanoparticle generates the photocurrent with an opposite polarization dependence on the NW end. This is because the nanoparticle is formed perpendicular to the axis of the Ag NW. Secondly, the photocurrent generation from the NW end exhibits similar intensity and polarization characteristics with and without the nanoparticle, which reveals the stability of our graphene SPP detector integrated with the Ag NW. We note that the robustness of the device can further be improved by covering it with a thin low-loss dielectric film such as SiO_2 or Al_2O_3.

In summary, we integrated a graphene photodetector with a single Ag NW and demonstrated an efficient detection of the long-range propagation SPPs. Polarization-resolved scanning photocurrent microscopy visualizes the localized excitation of SPPs at the end of the Ag NW, as well as verifies that the atomically thin graphene monolayer can effectively convert the evanescent field energy of SPPs to photocurrents. The responsivity of the graphene SPP detector is readily controlled by applied drain-source voltage; the estimated SPP detection responsivity at a drain-source voltage of 1 V is ~17 mA/W. We believe that our graphene SPP detector will be an important building block to integrate electronic and photonic elements, which can accomplish the realization of ultracompact nanophotonic and optoelectronic circuits.

Funding. National Research Foundation of Korea (NRF) (2017R1A2B2009117, 2017R1A4A1015426, 2018R1A3A-3000666, 2014M3A6B3063710, 2017R1D1A1B03033668).

REFERENCES

1. C. M. Lieber, MRS Bull. **36**, 1052 (2011).
2. R. W. Day, M. N. Mankin, R. Gao, Y.-S. No, S.-K. Kim, D. C. Bell, H.-G. Park, and C. M. Lieber, Nat. Nanotechnol. **10**, 345 (2015).
3. J. M. Lee, Y.-S. No, S. Kim, H.-G. Park, and W. I. Park, Nat. Commun. **6**, 6325 (2015).
4. T. Ozel, B. A. Zhang, R. Gao, R. W. Day, C. M. Lieber, and D. G. Nocera, Nano Lett. **17**, 4502 (2017).
5. J. Kim, H.-C. Lee, K.-H. Kim, M.-S. Hwang, J.-S. Park, J. M. Lee, J.-P. So, J.-H. Choi, S.-H. Kwon, C. J. Barrelet, and H.-G. Park, Nat. Nanotechnol. **12**, 963 (2017).
6. S. A. Maier, *Plasmonics: Fundamentals and Applications* (Springer, 2007).
7. M. L. Brongersma, N. J. Halas, and P. Nordlander, Nat. Nanotechnol. **10**, 25 (2015).
8. A. V. Akimov, A. Mukherjee, C. L. Yu, D. E. Chang, A. S. Zibrov, P. R. Hemmer, H. Park, and M. D. Lukin, Nature **450**, 402 (2007).
9. Y.-S. No, J.-H. Choi, H.-S. Ee, M.-S. Hwang, K.-Y. Jeong, E.-K. Lee, M.-K. Seo, S.-H. Kwon, and H.-G. Park, Nano Lett. **13**, 772 (2013).
10. K. C. Y. Huang, M.-K. Seo, T. Sarmiento, Y. Huo, J. S. Harris, and M. L. Brongersma, Nat. Photonics **8**, 244 (2014).
11. Y. Fang and M. Sun, Light Sci. Appl. **4**, e294 (2015).
12. A. L. Falk, F. H. L. Koppens, C. L. Yu, K. Kang, N. de Leon Snapp, A. V. Akimov, M.-H. Jo, M. D. Lukin, and H. Park, Nat. Phys. **5**, 475 (2009).
13. M. Esfandyarpour, E. C. Garnett, Y. Cui, M. D. McGehee, and M. L. Brongersma, Nat. Nanotechnol. **9**, 542 (2014).
14. M. L. Brongersma and V. M. Shalaev, Science **328**, 440 (2011).
15. F. Bonaccorso, Z. Sun, T. Hasan, and A. C. Ferrari, Nat. Photonics **4**, 611 (2010).
16. Q. Bao and K. P. Loh, ACS Nano **6**, 3677 (2012).
17. F. H. L. Koppens, T. Mueller, P. Avouris, A. C. Ferrari, M. S. Vitiello, and M. Polini, Nat. Nanotechnol. **9**, 780 (2014).
18. C.-H. Liu, Y.-C. Chang, T. B. Norris, and Z. Zhong, Nat. Nanotechnol. **9**, 273 (2014).
19. X. Wang, Z. Cheng, K. Xu, H. K. Tsang, and J.-B. Xu, Nat. Photonics **7**, 888 (2013).
20. F. Xia, T. Mueller, Y. Lin, A. Valdes-Garcia, and P. Avouris, Nat. Nanotechnol. **4**, 839 (2009).
21. X. Gan, R.-J. Shiue, Y. Gao, I. Meric, T. F. Heinz, K. Shepard, J. Hone, S. Assefa, and D. Englund, Nat. Photonics **7**, 883 (2013).
22. H.-S. Ee, H.-G. Park, and S.-K. Kim, Appl. Opt. **55**, 1029 (2016).
23. S.-K. Kim, H.-S. Ee, W. Choi, S.-H. Kwon, J.-H. Kang, Y.-H. Kim, H. Kwon, and H.-G. Park, Appl. Phys. Lett. **98**, 011109 (2011).